



# LUND UNIVERSITY

## Kerr Effect Tomography For Nonintrusive Spatially Resolved Measurements of Asymmetric Electric-field Distributions

Hertz, H. M

*Published in:*  
Applied Optics

*DOI:*  
[10.1364/AO.25.000914](https://doi.org/10.1364/AO.25.000914)

1986

[Link to publication](#)

*Citation for published version (APA):*

Hertz, H. M. (1986). Kerr Effect Tomography For Nonintrusive Spatially Resolved Measurements of Asymmetric Electric-field Distributions. *Applied Optics*, 25(6), 914-921. <https://doi.org/10.1364/AO.25.000914>

*Total number of authors:*  
1

### General rights

Unless other specific re-use rights are stated the following general rights apply:  
Copyright and moral rights for the publications made accessible in the public portal are retained by the authors and/or other copyright owners and it is a condition of accessing publications that users recognise and abide by the legal requirements associated with these rights.

- Users may download and print one copy of any publication from the public portal for the purpose of private study or research.
- You may not further distribute the material or use it for any profit-making activity or commercial gain
- You may freely distribute the URL identifying the publication in the public portal

Read more about Creative commons licenses: <https://creativecommons.org/licenses/>

### Take down policy

If you believe that this document breaches copyright please contact us providing details, and we will remove access to the work immediately and investigate your claim.

LUND UNIVERSITY

PO Box 117  
221 00 Lund  
+46 46-222 00 00

# Kerr effect tomography for nonintrusive spatially resolved measurements of asymmetric electric field distributions

Hans M. Hertz

An optical method for nonintrusive spatially resolved measurements of asymmetric electric field distributions in dielectric liquids is presented. Using multiangular Kerr effect measurements the electric field distributions are reconstructed with mathematical techniques known from computer-assisted tomography. The method is applicable to all high voltage devices containing liquids showing Kerr effect, allowing multiangular optical access, and having a relatively uniform electric field direction in the plane where the measurements are performed. The measurement technique is demonstrated experimentally with nitrobenzene. Comparisons between experimentally determined electric field distributions and theoretically calculated distributions show good agreement.

## I. Introduction

In high voltage applications optical Kerr effect measurements have been used for a long time to determine the electric field ( $E$ -field) in dielectric liquids such as nitrobenzene and transformer oil (Refs. 1 and 2 and references therein). Being a path integrating method, however, the spatial distribution of the  $E$ -field along the measurement path can only be determined if a special symmetry or geometry of the experimental arrangement is assumed. This paper presents a measurement technique to obtain 2-D spatially resolved electric field distributions in liquids that show Kerr effect. The  $E$ -field distribution is reconstructed from multiangular Kerr effect measurements by mathematical methods known from computer-assisted tomography.

Computer-assisted tomography is an established technique in x-ray imaging for medical and other purposes (e.g., Ref. 3). Here a 2-D map of the x-ray absorption of an object is reconstructed from measurements of the line integrals of the x-ray absorption for many rays crossing the object at different angles. However, the principle of tomography, i.e., using multiangular integrated measurements (projections) of a parameter in an object to produce a 2-D map of this

parameter, has applications in many other areas, for example, ultrasonic imaging, electron microscopy, and geophysics (Ref. 3 and references therein). Optical applications of tomography include studies on heat transfer<sup>4</sup> and combustion processes.<sup>5-7</sup>

Spatially resolved data of electric parameters such as potential,  $E$ -field, and space charge in dielectric liquids are of great importance, for example, in Kerr cell applications and in the design of oil insulated transformers. The electric field distribution (and thus also the other parameters mentioned above) can often be determined by theoretical calculations. However, surface flashover and similar problems often encountered demonstrate that the practical situation may not be fully theoretically understood. Thus measurements are needed both as a complement to the theoretical calculations and as an aid to improve the theoretical models. There are basically two techniques to measure electric fields in liquids, potential probe methods and optical methods based on the Kerr effect.<sup>8</sup> The potential probe method uses a small metal probe, insulated everywhere except at the tip, which is placed in the dielectric liquid. This method has the advantage of yielding point potential measurements. Through movements of the probe the  $E$ -field can be calculated using  $E = -\nabla U$ . A disadvantage is that the probe is in contact with the dielectric medium and may thus disturb the electric field distribution or cause breakdowns. Optical Kerr effect measurements are, like most optical techniques, nonintrusive and, therefore, do not disturb the electric field distribution. Furthermore, the sensitivity of the method increases at higher voltages due to the quadratic nature of the Kerr effect. The major disadvantage of Kerr effect

---

The author is with Lund Institute of Technology, Physics Department, P.O. Box 118, S-221 00 Lund, Sweden.

Received 26 October 1985.

0003-6935/86/060914-08\$02.00/0.

© 1986 Optical Society of America.

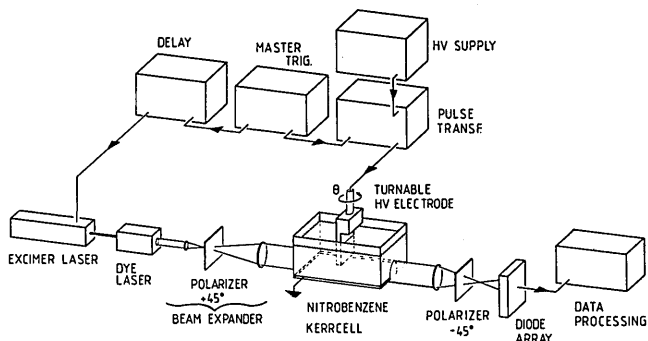


Fig. 1. Experimental arrangement. The high voltage electrode is enlarged for clarity.

measurements is that they yield path integrated data of the  $E$ -field. Thus spatially resolved  $E$ -field data can only be obtained assuming that either the  $E$ -field is constant and the geometry is known or the  $E$ -field is, for example, cylindrically symmetric.

In this paper 2-D spatially resolved asymmetric distributions of the electric field are reconstructed from multiangle optical Kerr effect measurements. The method combines the advantages of the two measurement methods mentioned above yielding spatially resolved data with increasing sensitivity at higher  $E$ -fields from nonintrusive measurements. With today's fast light detector and electronic technology time resolved measurements of the projections can be performed allowing measurements of the spatial and temporal development of, for example, electric fields and space charge accumulations.<sup>8</sup> The method is, like many other Kerr effect methods, restricted to determining the  $E$ -field distribution in a measurement plane where the direction of the  $E$ -field is relatively uniform.

The theory of the Kerr effect and the principles of tomographic reconstruction are briefly described in Secs. II and III. Section IV presents an experimental demonstration of the measurement method and typical results. A discussion of errors, including a comparison between experimentally recorded and theoretically calculated electric field distributions, is given in Sec. V. Finally, conclusions and a summary are presented in Sec. VI.

## II. Kerr Effect

The Kerr effect is described in any optics textbook (e.g., Ref. 9) and in more detail in, e.g., Ref. 10 and references therein. A brief description is given here. Under normal conditions a liquid is optically isotropic due to the statistically random orientation of the molecules. Application of an electric field aligns the molecules along the electric field direction producing an optically birefringent medium. Thus, if a light beam passes the liquid, the refractive index for light polarized parallel with the electric field direction is different from the refractive index for light polarized perpendicular to the field direction. The difference in refractive index  $\Delta n$  is

$$\Delta n = \lambda B E^2, \quad (1)$$

where  $\lambda$  is the wavelength of the light traversing the liquid,  $B$  is the Kerr constant, and  $E$  is the electric field in the liquid. The phase difference  $\delta$  between the parallel and perpendicular polarization components of the light after traversing the liquid is

$$\delta = 2\pi \int_0^L E(l)^2 B dl, \quad (2)$$

where  $L$  is the length of the Kerr cell, and the electric field is assumed to be dependent on the distance  $l$ . If the phase difference is assumed to be constant over a short distance  $l_0$ , the  $E$ -field can be calculated according to

$$E = \sqrt{\frac{\delta}{2\pi B l_0}}. \quad (3)$$

With an experimental arrangement such as the one depicted in Fig. 1 the phase shift can be detected. Assuming a vertical electric field, the first polarizer is oriented  $45^\circ$  to the electric field direction and the second polarizer perpendicular to the first. This converts the phase difference to an intensity modulation at the detector according to

$$I = I_0 A \sin^2(\delta/2), \quad (4)$$

where  $I_0$  is the incident light intensity,  $A$  accounts for light losses, and  $I$  is the intensity at the detector. Using, e.g., Eqs. (3) and (4) the  $E$ -field can be determined from intensity measurements.

The liquid used in the experiments described in Secs. IV and V was nitrobenzene because of its high Kerr coefficient. Other liquids such as water or oil also exhibit the Kerr effect, although the Kerr coefficient is 2 and 3, respectively, orders of magnitude lower than that of nitrobenzene.<sup>2,11</sup> Thus the same general methods demonstrated experimentally on nitrobenzene in this and other papers can in principle be used in studies of devices containing other liquids.

The accuracy of the calculated  $E$ -field is, of course, dependent on the accuracy of the length  $l_0$  and the Kerr coefficient  $B$  in Eq. (3). The length will be treated in Sec. V, and the Kerr coefficient is discussed briefly here following Ref. 10. The Kerr coefficient of nitrobenzene has been shown to depend on the frequency of the applied  $E$ -field, the wavelength of the incident light, and the temperature of the liquid. The frequency dependence is, however, less than  $\pm 1\%$  for frequencies below  $10^9$  Hz. The wavelength dependence is governed by the product  $B \cdot \lambda$ , which is constant within a few percent in the wavelength region from 630 to 500 nm. If a monochromatic light source such as a laser is used, the dispersion can be neglected, but the Kerr coefficient has still to be corrected for the difference between the laser wavelength and wavelength for which the Kerr coefficients are tabulated. The temperature dependence of the Kerr coefficient of nitrobenzene at  $\lambda = 632.8$  nm has been shown to be<sup>10</sup>

$$\frac{B(T)}{B(298 \text{ K})} = 8.085 - 5.450 \times 10^3 \cdot \frac{1}{T} + 9.954 \times 10^5 \cdot \frac{1}{T^2}. \quad (5)$$

Here the Kerr coefficients have been normalized to  $T = 298$  K.

For the experimental conditions of this paper ( $\lambda = 575$  nm,  $T = 295$  K) the Kerr coefficient is  $3.71 \times 10^{10}$  cm/V<sup>2</sup> according to Ref. 11. The accuracy of this value is  $\pm 6\%$ . However, other determinations of the Kerr coefficient given in the literature differ from the above value by nearly a factor of 2. Therefore, the constant was checked in the present paper using the same electrical and optical arrangement as in the tomographic measurements described below (Fig. 1) with the difference that the electrode system was exchanged for a parallel plate Kerr cell (see Ref. 1). With this electrode arrangement the  $E$ -field is uniform between the plates, and the geometry is well known. The influence of the electric field at the edges of the parallel plates was calculated and compensated for using the computer program described in Sec. V. This yielded a Kerr coefficient  $B = 3.82 \times 10^{-10}$  cm/V<sup>2</sup> at  $\lambda = 575$  nm and  $T = 294$  K. The tomographic experiments were performed at  $T = 295$  K making a small temperature correction according to Eq. (5) necessary giving the result  $3.77 \times 10^{-10}$  cm/V<sup>2</sup>. This value is expected to be correct within  $\pm 15\%$  and is in good agreement with the above value from Ref. 11.

### III. Tomographic Reconstruction Method

As mentioned in Sec. I, tomography is the general term for mathematical methods which reconstruct a 2-D map of a parameter from multiangular line integral measurements of the parameter (projections). Figure 2 shows the principal arrangement of the parallel beam geometry used in this paper.  $\delta(x,y)$  denotes the distribution of the parameter to be determined, and  $p(r,\theta)$  are the projections. In this paper each projection consists of many parallel line-integrated measurements of the phase difference induced by the Kerr effect [see Eq. (2)]. A 2-D map of the spatially resolved phase difference distribution  $\delta(x,y)$  is tomographically reconstructed using projections from different angles  $\theta$ . From this phase difference map the  $E$ -field distribution  $E(x,y)$  is calculated using Eq. (3).

In this paper the 2-D  $E$ -field distribution was reconstructed from only a few projections, i.e., with less information than in, for example, x-ray imaging. The use of few projection angles naturally limits the spatial resolution of the reconstructed picture. Suppose that the maximum spatial frequency of the phase difference field  $\delta(x,y)$  is denoted  $\zeta_{\max}$ ; i.e., the Fourier transform of  $\delta(x,y)$  equals zero for  $\zeta > \zeta_{\max}$ . It is calculated in Ref. 5 (and references therein) that the minimum number of angularly equally spaced projections  $M$  necessary to reconstruct a distribution  $\delta(x,y)$  having a maximum spatial frequency of  $\zeta_{\max}$  is

$$M = 2\pi\zeta_{\max}R, \quad (6)$$

where  $2R$  is the diameter of the reconstructed distribution. The equation is valid assuming an adequate SNR. In the experiments in this paper eight projection angles ( $M = 8$ ) were used to reconstruct a  $41 \times 41$ -pixel picture. Thus, if  $R \approx 25$  is assumed, the maxi-

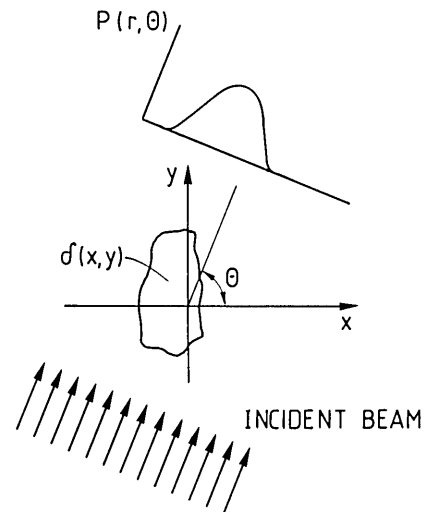


Fig. 2. Parallel beam geometry which was used in this experiment. The projections  $[p(r,\theta)]$  are the measured path integrated values of the phase difference field  $[\delta(x,y)]$  along the light path.

imum spatial frequency is  $\zeta_{\max} \approx 0.051$ ; i.e., the minimum spatial period for which one full sine wave is reconstructed correctly is  $1/\zeta_{\max} \approx 20$  pixels. A similar calculation to consider the bandlimiting effects of the limited number of equally spaced rays in each projection  $N$  yields

$$N = 4\zeta_{\max}R. \quad (7)$$

In this paper, however, Eq. (7) does not affect the bandlimit because each projection used in the tomographic reconstruction consisted of approximately fifty rays effectively. This results in a bandlimit of  $\zeta_{\max} \approx 0.50$ , which is negligible compared to the bandlimit imposed by the limited number of projection angles. For the rather smoothly varying  $E$ -field distributions encountered in the experiments of Secs. IV and V (see Figs. 6 and 7) it is anticipated that eight projection angles yield approximately sufficient spatial resolution. However, for each new measurement situation the required number of angular projections and number of rays in each projection have to be calculated to obtain the desired spatial resolution.

A general review of different tomographic reconstruction methods is given by Herman<sup>12</sup> and in Ref. 3. The two major groups of algorithms are the convolutional backprojection and Fourier transform methods and the iterative methods. The first group, which has been successfully used in medical x-ray imaging, has the advantage of being computationally simple and fast. They are, however, not suited for reconstruction problems having few projection angles. The iterative methods are computationally slower but appear superior to the first group in treating systems with few projections (Ref. 13 and references therein). In the present paper algebraic reconstruction technique (ART) algorithms are used.<sup>14</sup> These algorithms iteratively adjust an estimation of  $\delta(x,y)$  by comparing projections calculated from the estimated  $\delta(x,y)$  with the corresponding experimental projections until conver-

gence is accomplished. Because few projection angles are used, the reconstruction problem is highly underdetermined; i.e., there are many solutions  $\delta(x,y)$  that fulfill the constraints of the projections. The different ART algorithms converge at different solutions, each optimizing some criterion for the reconstructed image given the constraints of the projections. In this paper the multiplicative ART (MART) algorithm,<sup>14</sup> which has been shown to converge at the maximum entropy solution,<sup>15</sup> was used.

Below the reconstruction procedure of MART is briefly described using the notation of Ref. 14. At the start of the iterative procedure each picture element (pixel) is given a nonzero value. The picture is then reconstructed iteratively, one typical step being

$$\delta_i^{q+1} = \left( \frac{p_j}{p_j^q} \right)^{w_q} \cdot \delta_i^q. \quad (8)$$

Here subscript  $i$  denotes the pixels, and subscript  $j$  refers to the projection channels.  $\delta_i$  are the phase difference values of each pixel,  $p_j$  are the experimental projection data, and  $p_j^q$  are the calculated projection data from the reconstructed picture after the  $q$ th iteration.  $w_q$  is a relaxation factor.

The original MART algorithm has been modified to reduce reconstruction artifacts. The modifications include (1) exact discretion, i.e., the overlap between the projection rays and each pixel is calculated exactly; (2) variable underrelaxation; and (3) random selection of the order in which the projections are chosen in the iterative process. The first modification suppresses streaking artifacts known to occur in ART-type algorithms, and the second and third reduce the negative influence of noise and inconsistencies in the experimental projection data. These modifications are important, especially in areas of the picture where the  $E$ -field is relatively low. This is because the  $E$ -field is proportional to  $\sqrt{\delta}$  [see Eq. (3)], and, thus, when the phase difference data  $\delta(x,y)$  are inverted to  $E$ -field data, small reconstruction errors in the phase difference map influence the  $E$ -field map more strongly in the low  $E$ -field areas than in the high  $E$ -field areas.

#### IV. Experimental Procedure and Results

In this section the method described above is demonstrated experimentally. The experimental arrangement is shown in Fig. 1. A pulse transformer produced 30- $\mu$ s long high voltage pulses with a 10-Hz pulse repetition frequency. The pulses were fed to the turnable 4- $\times$ 20-mm brass electrode (see Fig. 1), which was asymmetrically positioned in a nitrobenzene filled reservoir (Kerr cell) 2.8 mm above a flat grounded bottom plate. The voltage pulses were measured with a commercial high voltage probe connected to an oscilloscope. Pulsed voltages were used instead of dc voltages to avoid problems with accumulating space charges and the turbulence well known to occur in nitrobenzene that has not been carefully purified.<sup>1</sup>

The light source used in this experiment was an excimer laser pumped dye laser (Lambda Physik) which emitted sufficient monochromatic pulses at  $\lambda =$

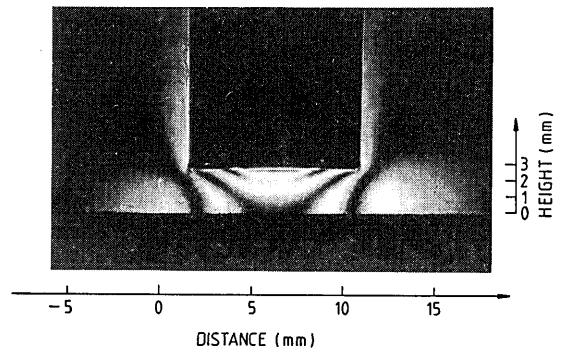


Fig. 3. Intensity pattern at the detector plane for  $\theta = 112.5^\circ$ . The fringes were recorded 0.5 mm above the bottom plate.

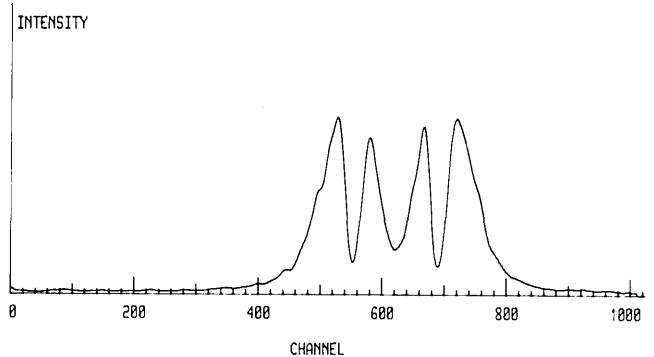


Fig. 4. Typical intensity distribution recorded by the 1024-channel diode array at  $\theta = 112.5^\circ$ .

575 nm. The laser beam had to be strongly attenuated not to saturate the detector. The short pulse duration (15 ns) ensures that the pulsed  $E$ -field in the Kerr cell is stable during exposure of the light pulse. After expanding the beam to  $\sim 9$ -cm diameter it illuminated the Kerr cell, which was placed between crossed polarizers. A lens images the intensity distribution on a horizontally mounted linear diode array detector with 1024 diodes (Reticon). Figure 3 shows a typical intensity distribution at the detector at a projection angle of  $\theta = 112.5^\circ$ . The diode array detected the fringes  $\sim 0.5$  mm above the bottom plate. In Fig. 4 a typical recording by the diode array for  $\theta = 112.5^\circ$  is shown.

The experimental recordings were evaluated assuming that the electric field was vertical, i.e., perpendicular to the bottom plate at the recording level 0.5 mm above the bottom plate. This was experimentally confirmed by observing the intensity pattern with the first polarizer vertically and the second horizontally oriented. With this orientation no phase shift between the two polarization states is induced if the  $E$ -field is vertical, and thus no light is transmitted through the second polarizer. In this case the  $E$ -field was observed to be nearly vertical up to  $\sim 0.75$  mm above the bottom plate. Deviations from the vertical field direction up to  $\pm 10^\circ$  were observed in the measurement plane below the edges of the electrode. The influence of this deviation on the measurement accuracy is discussed in the next section.

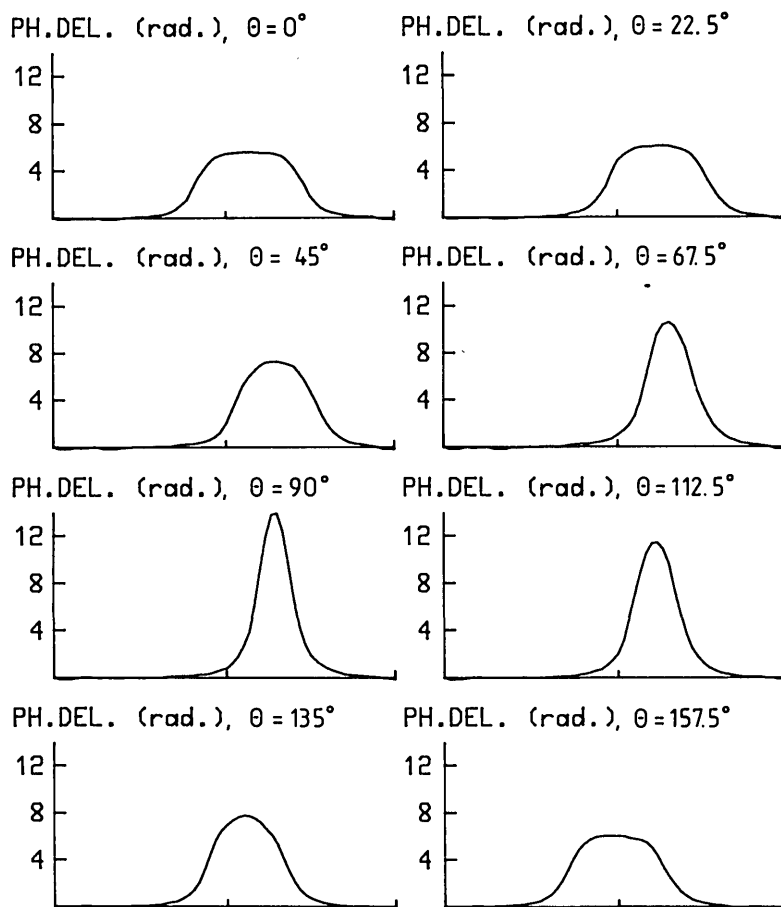


Fig. 5. Total phase delay for all eight projections.

The experimental recordings of Fig. 4 were stored on floppy disks and transferred to a NORD 500 minicomputer. Evaluation of the recordings and the mathematical processing leading to a 2-D  $E$ -field map were performed with an interactive computer program. The total phase delay of the projections is calculated assuming the  $\sin^2$  intensity dependence of Eq. (4). Figure 5 shows the total phase delay in radians for all eight projections. Before the tomographic reconstruction the 1024 channel projections were reduced by averaging to 61 channels to reduce reconstruction computer time. The modified MART algorithm applied to these projections produces a 2-D phase difference map in a  $41 \times 41$ -pixel picture. Knowing the size of each pixel ( $l_0 = 1.045$  mm) the  $E$ -field distribution is calculated from the phase difference map using Eq. (3). Figure 6 shows the  $E$ -field distribution in a plane 0.5 mm above the bottom plate; 17.2 kV was applied to the  $20 \times 4$ -mm electrode, and the distance between the electrode and bottom plate was 2.8 mm. The maximum  $E$ -field in the reconstruction is 51 kV/cm.

The wavelike surface of the low  $E$ -field areas of the picture is due to small reconstruction errors in the phase difference map that have been amplified through Eq. (3) as discussed in Sec. III. The flat areas

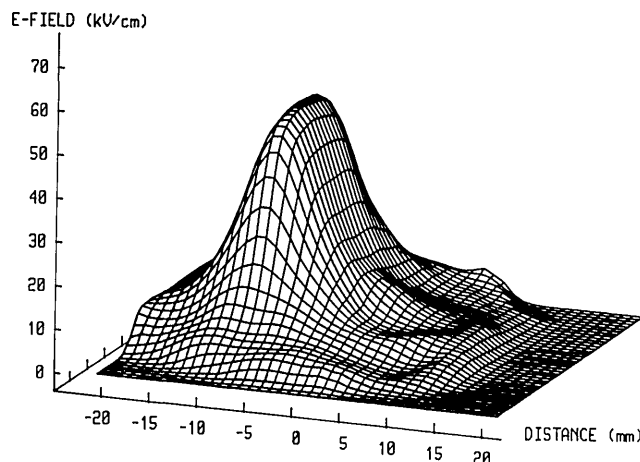


Fig. 6. Experimental determination of the  $E$ -field distribution in nitrobenzene in a plane between a rectangular HV electrode and a semi-infinite grounded plane.

of the zero  $E$ -field in Fig. 6 are due to the inherent discrimination of negative reconstruction values in the MART algorithm. The accuracy and errors of this reconstruction are discussed in more detail in the next section.

## V. Measurement Accuracy

To estimate the accuracy of the  $E$ -field measurements presented in the previous section, similar measurements were performed with a cylindrical electrode. Due to the cylindrical symmetry of this experimental arrangement, the  $E$ -field could be calculated theoretically for comparison to the experimental results. The measurements and reconstructions were performed according to the description in Sec. IV except for the exchange of the rectangular electrode for a cylindrical electrode of 20-mm diameter. The voltage on the electrode was 14.3 kV, and the distance between the electrode and bottom plate was 2.3 mm. Figure 7 shows the reconstructed  $E$ -field 0.5 mm above the bottom plate. The center of the cylindrically symmetric distribution is positioned slightly behind the center of the picture.

It is well known from any textbook on electromagnetic field theory (e.g., Ref. 16) that the potential field in a dielectric medium is determined by Poisson's equation:

$$\nabla^2 U = \rho / \epsilon \epsilon_0, \quad (9)$$

where  $\nabla^2$  is the Laplace operator,  $U$  is the potential,  $\rho$  is the space charge density,  $\epsilon$  is the relative permittivity, and  $\epsilon_0$  is the permittivity of free space. Other Kerr effect experiments<sup>8</sup> have shown that space charges start to develop  $\sim 100 \mu\text{s}$  after application of the electric field. In this experiment the laser pulse exposed the Kerr cell 15  $\mu\text{s}$  after the start of the voltage pulse. Thus the space charges can be neglected here, and Eq. (9) is reduced to the Laplace equation:

$$\nabla^2 U = 0. \quad (10)$$

When the potential  $U$  has been determined from Eq. (9) or (10) the  $E$ -field can be calculated according to

$$E = -\nabla U. \quad (11)$$

The Poisson and Laplace equations cannot normally be solved analytically in three dimensions. Fortunately, a user friendly computer program that solves these equations numerically for cylindrically symmetric geometries was readily available from the Department of Theoretical Physics at the Lund Institute of Technology.<sup>17</sup> Normally this program is used for studies of 3-D heat flows and temperature fields. These phenomena are governed by the same basic equations as the electric field and the electric potential. The program, which will not be discussed in detail here, iteratively converges toward a solution to Eq. (9) given a set of boundary conditions. In this case the boundary conditions were 14.3 kV at the electrode and 0 kV at the bottom plate. Furthermore, it was assumed that far from the electrode the derivative of  $U$  in the radial  $r$ -direction is 0 ( $\partial U / \partial r = 0$ ), and far from the bottom plate the same is assumed for the vertical  $z$ -direction ( $\partial U / \partial z = 0$ ). The result of the calculation is shown in Fig. 8, where it is depicted in the same type of figure as used in the experimental work for comparison. The center of the calculated cylindrically symmetric distribution is positioned at the same coordi-

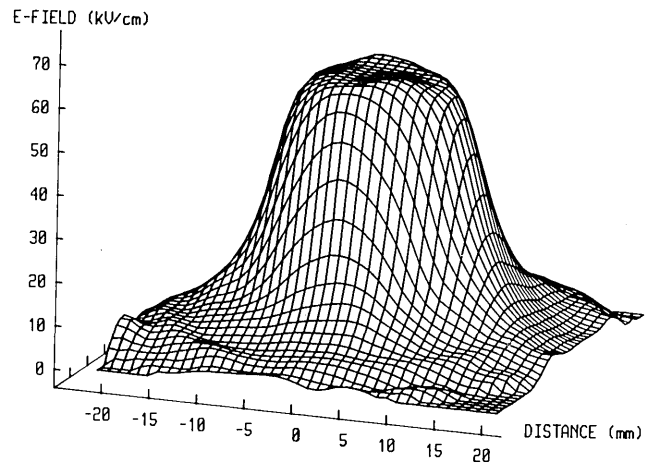


Fig. 7. Experimentally reconstructed  $E$ -field distribution from a cylindrical HV electrode over a semi-infinite grounded plane.

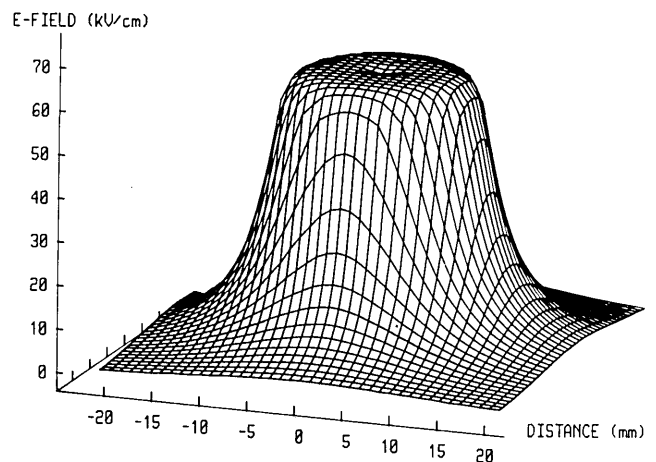


Fig. 8. Theoretically calculated  $E$ -field distribution for a geometry corresponding to the experimental determination of Fig. 7.

nates as the center of the experimental distribution of Fig. 7. In Fig. 9 the experimental and theoretical  $E$ -field data are compared assuming cylindrical symmetry. The full line depicts the calculated  $E$ -field, and the dots are the experimentally reconstructed  $E$ -field values as a function of distance from the center of the distributions in Figs. 7 and 8. The agreement between the experimental and theoretical  $E$ -field values is very good, although there are some differences in the shape of the curvature at the edge of the electrode ( $r \approx 10$  mm). This deviation will be discussed below.

The theoretically calculated  $E$ -field values of the flattop are primarily determined by the ratio  $U_0/d$ , where  $U_0$  is the voltage and  $d$  is the distance between the electrode and bottom plate. In the experimental recording the voltage was measured to be  $U_0 = 14.3 \pm 1.0$  kV and the distance  $d = 2.3 \pm 0.1$  mm. The theoretical and experimental results agree well within these error limits.

The difference in shape of the curvature in Fig. 9 at the edge of the electrode is probably primarily because the direction of the  $E$ -field was not perfectly vertical at

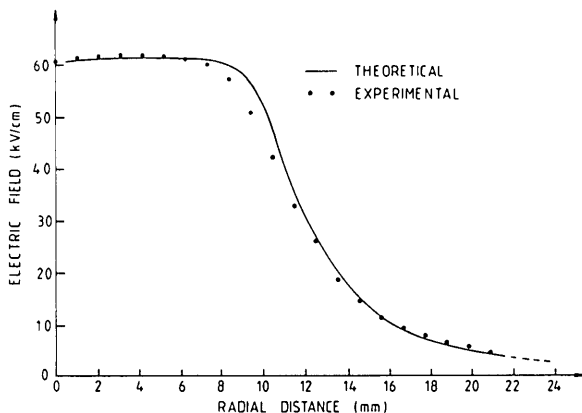


Fig. 9. Comparison between the experimental (dots) and the theoretical (full line)  $E$ -field determinations for the cylindrically symmetric distributions of Figs. 7 and 8.

all positions in the measurement plane, i.e., not fully perpendicular to the bottom plate 0.5 mm above the bottom plate. As mentioned above, a deviation of  $10^\circ$  was observed experimentally near the edges of the rectangular electrode. The same experimental observation was made with the cylindrical electrode, and the theoretical calculations confirm a deviation of  $10^\circ$  near the edges of that electrode. This reduces the measured phase difference in the edge region and thus lowers the experimental values around the electrode edge in Fig. 9. Another factor that might influence the shape of the  $E$ -field reconstruction in the edge region is that only eight projections are used, and thus the highest spatial frequencies might be somewhat suppressed.

Some additional sources of error in the experimental reconstruction procedure should be mentioned. Although these errors are discussed with reference to the experimental arrangement used in this paper they are of general interest for any experimental studies using Kerr effect tomography.

(1) As mentioned in Sec. III, reconstruction errors in the low  $E$ -field areas of the phase difference map are amplified when they are inverted to  $E$ -field values using Eq. (3) due to the square root dependence of  $E$  on  $\delta$ . This is easily observed in Figs. 6 and 7, where the well-known streaking effects of the ART-type algorithms induce errors in the phase difference map, which are then amplified to a wavelike surface. The reconstruction errors in the low levels of the phase difference map was  $\sim 1$ –2% of the peak phase difference value. These errors are then amplified through Eq. (3) to 10–15% of the peak  $E$ -field value. These reconstruction artifacts are obviously reduced if a larger number of projection angles are used. Contrary to the situation in the low  $E$ -field areas, the peak  $E$ -field values are very insensitive to reconstruction noise due to the square root dependence of Eq. (3).

(2) Due to the relatively low resistance of unpurified nitrobenzene, the liquid between the electrode and bottom plate will be heated. This creates a thermal lens, which deflects the laser beam. In the measurements with the cylindrical electrode in this experi-

ment, the deflections were negligible. Using the rectangular electrode, however, the deflection clearly influenced the projection at  $\theta = 90^\circ$  leading to a somewhat wider projection profile than actually should have been the case. As the other projections were much less affected, this error is not expected to have influenced the reconstructed  $E$ -field distribution substantially.

(3) As mentioned in Sec. II, the Kerr coefficient is dependent on the temperature of the nitrobenzene. The temperature in the liquid between the electrode and bottom plate was measured with a copper-constantan thermocouple. It was determined to be  $295 \pm 0.5$  K. The Kerr coefficient for this temperature was determined in Sec. II to be  $B = 3.71 \times 10^{-10}$  cm  $V^{-2} \pm 6\%$ . Heating due to the applied voltage pulses was  $< 1$  K with the cylindrical electrode. The error in the Kerr coefficient due to this and other temperature variations during the experiment is expected to be less than  $\pm 2\%$ .

(4) The pixel size was determined to be  $l_0 = 1.045$  mm  $\pm 5\%$ . This error is mainly due to aberrations in the imaging and the light detection system, which results in a somewhat nonuniform pixel size.

However, the errors in the Kerr coefficient  $B$  and in the pixel size  $l_0$  do not impair the accuracy of the reconstructed  $E$ -field very much. Due to the square root dependence of Eq. (3) the relative error in the  $E$ -field only carries half of the relative errors in  $B$  and  $l_0$ . Thus these errors are mostly small, especially in the low  $E$ -field areas, compared with the reconstruction errors discussed above. The opposite situation might occur, especially in the high  $E$ -field areas, if many projection angles were used. Then the streaking and noise-induced reconstruction artifacts would be reduced.

## VI. Summary and Conclusions

In this paper a nonintrusive optical method to measure 2-D distributions of electric fields in dielectric liquids has been presented. The 2-D  $E$ -field distribution is reconstructed from multiangular Kerr effect measurements with mathematical algorithms developed in computerized tomography. The method assumes a relatively uniform field direction in the plane where the  $E$ -field distribution is to be measured. Although the measurement technique was demonstrated on a special experimental arrangement it is a general method for measurement of  $E$ -field distributions in any high voltage device that contains a liquid showing the Kerr effect and allows multiangular optical access. In liquids having low Kerr coefficients (e.g., oil) the projection data have to be measured with more sensitive techniques than have been done here (e.g., Ref. 18).

In many practical situations, however, it is not possible to obtain complete projection data because opaque objects block the optical access. Such limitations of, e.g., the accessible projection angles naturally reduce the spatial resolution of the reconstruction. For such situations it should be noted that special algorithms

for tomographic reconstruction from incomplete projection data have been developed (e.g., Ref. 19).

The major sources of error in this experiment are a somewhat nonuniform  $E$ -field direction in the measurement plane and reconstruction errors due to streaking artifacts and noise in the projection data. The reconstruction errors primarily affect the low  $E$ -field values. This would be reduced if a greater number of projection angles were used.

Spatially resolved  $E$ -field measurements are important in many applications such as the general understanding of the electric properties of dielectric liquids and in the design of high voltage devices such as, e.g., Kerr cells for voltage measurements and high voltage transformers. In the latter case the method should be important in locating regions of greatest electrical stress where breakdowns are more likely to occur. Furthermore, with multiangular experimental configurations allowing simultaneous recording of the different projections, the transient buildup of an electric field in a single event could be measured. Studies of the spatial and temporal distribution of space charges and their influence on the  $E$ -field distribution are also feasible. Excellent time resolution can be obtained using pulsed laser light sources.

The author is indebted to S. Borgström for his advice concerning construction of the high voltage pulse transformer and to B. Efring, who generously gave me access to and introduced me to the computer program used for the theoretical calculations. The constant support and guidance of G. Holmstedt and S. Svanberg are highly appreciated.

## References

1. E. C. Cassidy, R. E. Hebner, M. Zahn, and R. J. Sojka, "Kerr Effect Studies of an Insulating Liquid under Varied High-Voltage Conditions," *IEEE Trans. Electron. Inst.* **EI-19**, 43 (1974).
2. E. F. Kelley and R. E. Hebner, "Electro-optic Measurement of the Electric Field Distribution in Transformer Oil," *IEEE Trans. Power Apparatus Syst.* **PAS-102**, 2092 (1983).
3. Special Issue on Computerized Tomography, *Proc. IEEE* (Mar. 1983).
4. D. W. Sweeney and C. M. Vest, "Measurements of Three-Dimensional Temperature Fields above Heated Surfaces by Holographic Interferometry," *Int. J. Heat Mass Transfer* **17**, 1443 (1974).
5. P. J. Emmerman, R. Goulard, R. J. Santoro, and H. G. Semerjian, "Multiangular Absorption Diagnostics of a Turbulent Argon-Methane Jet," *J. Energy* **4**, 70 (1980).
6. K. E. Bennett, G. W. Faris, and R. L. Byer, "Experimental Optical Fan Beam Tomography," *Appl. Opt.* **23**, 2678 (1984).
7. H. M. Hertz, "Experimental Determination of 2-D Flame Temperature Fields by Interferometric Tomography," *Opt. Commun.* **54**, 131 (1985).
8. Z. Croitoru, "Space Charges in Dielectrics," in *Progress in Dielectrics, Vol. 6*, J. B. Birks and J. Hart, Eds. (Temple Books, London, 1965).
9. E. Hecht and A. Zajac, *Optics* (Addison-Wesley, Reading, Mass., 1979).
10. R. E. Hebner, R. A. Malewski, and E. C. Cassidy, "Optical Methods of Electrical Measurement at High Voltage Levels," *Proc. IEEE* **65**, 1524 (1977).
11. R. E. Hebner, "Kerr Coefficients of Nitrobenzene and Water," National Bureau of Standards Report NBSIR 74-44 (1974).
12. G. T. Herman, *Image Reconstruction from Projections* (Academic, New York, 1980).
13. G. Minerbo, "MENT: A Maximum Entropy Algorithm for Reconstructing a Source from Projection Data," *Comput. Graph. Image Process.* **10**, 48 (1979).
14. R. Gordon, "A Tutorial on ART," *IEEE Trans. Nucl. Sci.* **NS-21**, 78 (1974).
15. A. Lent, "A Convergent Algorithm for Maximum Entropy Image Restoration, with a Medical X-ray Application," in *Image Analysis and Evaluation*, R. Shaw, Ed. (Society of Photographic and Scientific Engineers, Washington, D.C., 1977), p. 249.
16. P. Lorrain and D. Corson, *Electromagnetic Fields and Waves* (Freeman, San Francisco, 1970).
17. B. Efring, Department of Theoretical Physics, Lund Institute of Technology; personal communication.
18. A. Törne and U. Gäfvert, "Measurement of the Electric Field in Transformer Oil Using Kerr Technique with Optical and Electrical Modulation," in *Proceedings, ICPADM, Vol. 1*, Xian China, 24-29 June 1985, p. 61.
19. C. M. Vest and I. Prikyl, "Tomography by Iterative Convolution: Empirical Study and Application to Interferometry," *Appl. Opt.* **23**, 2433 (1984).

## NEW GLASS STANDARDS CERTIFIED FOR CHEMICAL CONTENT

The chemical composition of glass determines the material's properties such as thermal performance, resistance to radiation, electrical conductivity, and durability. Glass manufacturers and the designers of glass products who require specific material performance will be interested in three new standard reference materials (SRMs) for use in evaluating chemical methods of analysis and in calibrating instruments to analyze the chemical content of glass. SRM 1411, Soft Borosilicate Glass and SRM 1412, Multicomponent Glass are 10 platelets and 8 platelets respectively, and are about 30-millimeters square. SRM 1413, High Alumina Sand is a 75-gram unit tested for homogeneity. The SRMs may be purchased for \$172 per unit from the Office of Standard Reference Materials, B311 Chemistry Building, National Bureau of Standards, Gaithersburg, Md. 20899, telephone: 301/921-2045.